*Progress In Electromagnetics Research C, Vol. 100, 145–159, 2020*

# Efficient Simulation Tool to Characterize the Radar Cross Section of a Pedestrian in Near Field

**Giovanni Manfredi[1, *], Paola Russo[2], Alfredo De Leo[2], and Graziano Cerri[2]**

**Abstract**—A simulation tool to characterize the radar cross section of a pedestrian in near field is presented in the paper. The tool has been developed in order to predict and optimize the performance of the short-range radar systems employed in autonomous vehicle operations. It is based on an analytical model which joins the modeling of the human body with the theory of the physical optics. Our studies first focused on the implementation of the electromagnetic code where the human body, the radiation properties of the antenna, and the scenario to be analyzed have been analytically expressed. Then, the proposed model has been validated in terms of accuracy comparing simulated, theoretical, and experimental data regarding the radar cross section of metal and lossy spheres and of an adult, in the frequency range 23–28 GHz. In the end, an evaluation of the performance in terms of required computer memory and execution time has been carried out, comparing the proposed simulation tool with other numerical computational methods.

## 1. INTRODUCTION

In recent years, the development of autonomous emergency breaking (AEB) systems has increased in the automotive industry. These technologies are largely deployed to improve road safety levels and ease the driver's workload [1]. The AEB systems installed in numerous vehicles [2] use the combination of camera sensors and radar sensors to identify potential pedestrian collision ahead of the car. Cameras are the main sensors for detecting pedestrians. Radars are employed for measuring the distance and the occupying area of the subject [3–5]. Ultra-Wide Band (UWB) radar system, for instance, is a technology widely used for human tracking due to its advantages in poor visibility and mainly for the employed wide bandwidth signals which enable high-resolution in ranging and localization [6–8].

The assessment of the performance of the radars makes the analysis of the radar cross section (RCS) of the human body a topic of a great interest [9–11]. Fortuny-Guasch has presented the results of an extensive series of RCS measurements on pedestrian dummies and humans, analyzing the influence of their dimensions and the effect of clothing in the 24 GHz and 77 GHz bands [15].

Since the postures and shapes of the pedestrians are endless, the numerical modeling of the RCS of a human body proves more suitable for the performance analysis of the radar systems. Le and Dogaru [16, 18] have simulated the radar cross section of standing men in the UHF-band (0.3–0.5 GHz), L-band (1.2–1.5 GHz), Ku-band (15.2–18.3 GHz), and Ka-band (33.4–38.6 GHz). The Finite-Difference Time Domain (FDTD) and Xpatch have been used as electromagnetic (EM) modeling codes for their studies. FDTD is an exact technique but computationally intensive; therefore, it has been run in the lower frequency bands (UHF and L). Xpatch combines the theory of the ray tracing with the theory of the physical optics, and it proves to be suitable for the high frequency analysis and for the modeling of scenarios involving large problem space. The approximate solver provides accurate

---

*Received 27 November 2019, Accepted 5 March 2020, Scheduled 11 March 2020*

* Corresponding author: Giovanni Manfredi (giovanni.manfredi@centralesupelec.fr).
[1] SONDRA, CentraleSupélec, Université Paris-Saclay, F-91190 Gif-sur-Yvette, France. [2] Department of Information Engineering, Università Politecnica delle Marche, Ancona 60131, Italy.

results in considerably less time than the FDTD algorithm [18], but it computes the backscattered field using a plane-wave (PW) excitation. The frequency bands for the radar applications devoted to the collision avoidance and to the adaptive cruise control are 24–24.25 GHz and 77–81 GHz, respectively [19]. Hamdane et al. have shown in [20] that the pedestrians are located by the radars less than 20 m from the front of the vehicle. This distance identifies a near field region, considering the high working frequencies and the dimension of the human targets [21–24], where the PW condition is not verified. It follows that the implementation of the antenna is needed at the numerical modeling stage for the evaluation of the RCS. It allows the designer to analyze the influence of the radar parameters such as the radiation pattern, the operating frequencies, and the distance between the radar and the monitored target on the calculated RCS.

The deeper understanding of the interaction between the EM waves and the human body also requires 3D models that match real subjects with a high degree of accuracy. Many phantoms have been developed with different geometries, number of tissues, dielectric properties, and voxel precision [25–28]. Chen et al. [32] performed a numerical RCS analysis at 76–77 GHz of a pedestrian modelled by using the software Pozer 9. A correction for the overlapped meshes has been carried out to improve the simulation speed of the EM software FEKO$^{\text{TM}}$. Van Dorp and Groen [29] and Mohamed et al. [30] presented a simplification of the human shape by using cylinders of various sizes to compose the body parts. However, to our knowledge, very few studies have been done to assess the features and accuracy of the presented 3D models used in scattering problems. They are not always compatible with the EM codes and with the dimensions or postures of the human target that has to be analyzed. Furthermore, the meshes, discretizing the exterior shell of the body, are built, either automatically by the EM simulators [16, 17] or by using an external software package [31]. These represent relevant constraints for the radar designer who is limited in reaching the best trade-off between required computational resources and EM code accuracy [32, 33].

The authors present in the paper an EM code that includes, in a single simulation tool, the analytical modeling of the human body, of the antenna, and of the characterization of the back scattered field. The aim is to release a tool sufficiently accurate, fast, and light from the point of view of computational burden, which makes feasible the modeling of scenarios involving large problem space, without the need of high performance computing (HPC) systems. In detail, the human body is modeled by canonical geometries by using the cuboid equation, making the model suitable for all dimensions and postures of any target that has to be analyzed. The incident field is radiated by whatever antenna can be implemented both to reproduce a real scenario and to analyze its influence in the propagation and reflection phenomenon. The backscattered response of the body is provided by an EM algorithm based on the theory of the physical optics.

The calculation of the RCS of metal and lossy spheres and of a potential pedestrian has been carried out in the frequency range 23–28 GHz in order to establish the accuracy of the EM code. To this purpose, the simulated results have been compared with the theoretical ones based on the Mie theory [12–14] and with the measured data provided by the European Commission Joint Research Centre [15]. Then, a performance assessment of the proposed simulation tool has been performed and compared with those of FEKO$^{\text{TM}}$ by using the FDTD and Multilevel Fast Multipole Method (MLFMM) solutions.

The paper is organized as follows. The analytical model founded on the generation of the human body model, on the geometric typesetting of the real scenario under observation and on the computation of the total fields scattered by the target, is analyzed in Section 2. The simulated and experimental data relative to the characterization of the RCS of the spheres and of the human target are compared and commented in Section 3. The performance assessment is shown in Section 4. The conclusions are presented in Section 5. In the end, the details concerning the computation based on the theory of the physical optics are provided in the Appendix.

## 2. EM CODE FOR THE PEDESTRIAN RCS CHARACTERIZATION

In this section, the human body and the geometry of the scenario of interest are defined. Then, the procedure to characterize the scattered field by a real target is presented. All the quantities are analytically determined and implemented in MATLAB® software.

### 2.1. Human Body Model

Previous works [34, 35] have pointed out that the accurate representation of external details of the body, such as the nose, mouth, ears, and fingers, can be neglected for the evaluation of the scattered field. This means that the human body parts (head, chest, arms, and legs) can be modeled as a collection of canonical geometries by using the following function:

$$f(x, y, z) = \left(\frac{x - x_g}{a}\right)^m + \left(\frac{y - y_g}{b}\right)^n + \left(\frac{z - z_g}{c}\right)^p = 1 \tag{1}$$

Equation (1) represents the surface of a cuboid in a 3D space, where $x_g, y_g, z_g$ are coordinates of the center of the geometric shape; $a, b, c$ are the semi-length, semi-width, and semi-height, respectively, of the geometric shape; and $m, n, p$ are coefficients which define the curvature of the surface for each axis. By means of the proper choice of parameters $a, b, c, m, n, p$ listed in Table 1, a human model has been modelled as having 13 body parts, reproduced by the combination of a sphere, cylinders, and a parallelepiped. The chosen dimensions are equivalent to the average human body size [24]. In addition, rotation matrices have been implemented in order to simulate movements and variations of the body postures, as shown in Fig. 1. Moreover, starting from 18 GHz and moving to higher frequencies, the

**Table 1.** Human model parameters.

| Human Element | $a$ (cm) | $b$ (cm) | $c$ (cm) | $m$ | $n$ | $p$ | Shape |
|---|---|---|---|---|---|---|---|
| Head ($H$) | 10 | 10 | 10 | 2 | 2 | 2 | Sphere |
| Neck ($N$) | 5.5 | 5.5 | 6 | 2 | 2 | 10 | Cylinder-like |
| Torso ($T$) | 16 | 8 | 23 | 15 | 15 | 15 | Ellipsoid-like |
| Upper Arm ($UA$) | 6 | 6 | 15 | 2 | 2 | 20 | Cylinder-like |
| Lower Arm ($LA$) | 5 | 5 | 15 | 2 | 2 | 20 | Cylinder-like |
| Upper Leg ($UL$) | 7 | 7 | 24 | 2 | 2 | 20 | Cylinder-like |
| Lower Leg ($LL$) | 6 | 6 | 22 | 2 | 2 | 20 | Cylinder-like |
| Feet ($F$) | 4.5 | 15.5 | 2 | 2 | 2 | 20 | Cylinder-like |

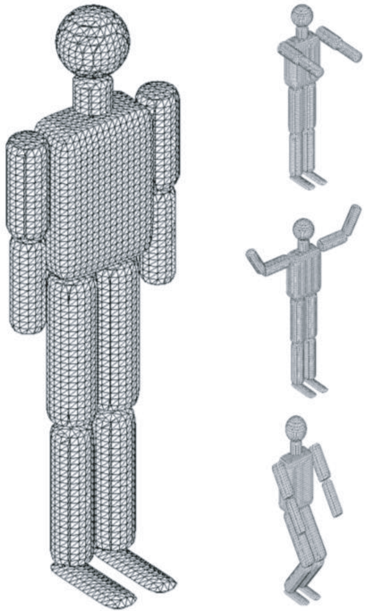

**Figure 1.** Human body model analytically expressed and implemented in MATLAB® in several positions. The triangular meshes adopted to discretize the body surface are also shown.

field penetration depth is lower than 1.5 mm [36, 37]. Consequently, only the skin dielectric parameters to model the interaction between the body and EM fields are considered.

### 2.2. Geometry of the Scenario under Observation

The EM model consists of evaluating a proper equivalent surface current distribution from which the scattered field is calculated [38, 39]. In order to represent the fields involved in the problem, the geometry of the scenario to describe the interaction between the body and the wave front is first of all defined. Fig. 2 depicts the antenna $A$, represented by an aperture antenna, the fixed Cartesian system $(O, x, y, z)$ centered on the aperture, and the scattering surface element $S$. The subarea is a triangular patch surface mesh, which discretizes the radiated body parts. Its dimensions are inferior to $\lambda/10$ at the highest work frequency, to obtain an accurate solution.

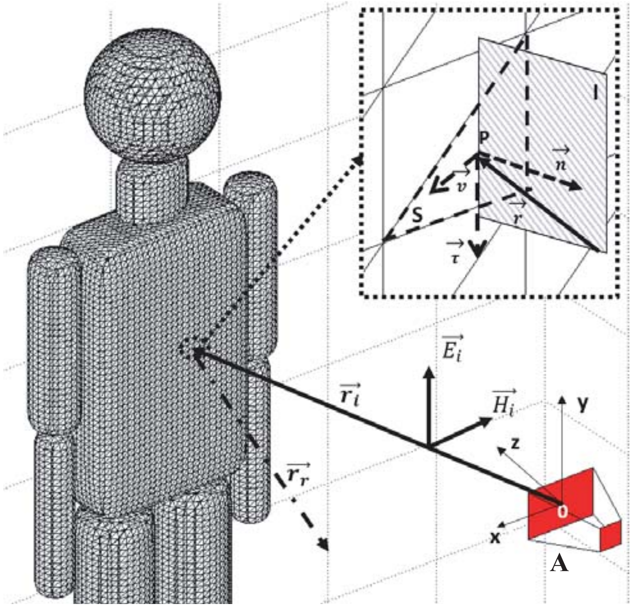

**Figure 2.** Geometry representation of the scenario involved in the interaction between the body surface element $S$ (triangular patch) and the antenna.

### 2.3. Incident and Scattered Fields Computation

The field radiated by the antenna and impinging on the body is obtained by the auxiliary electric potential vector $\vec{F}$ [40], assuming a known distribution of the aperture antenna field

$$\vec{E}_A = E_0 \cos\left(\frac{\pi x}{A_W}\right)\hat{y} \tag{2}$$

$A_W$ represents the width of the aperture antenna. $E_0$ denotes the maximum intensity of the aperture electric field, and it is calculated by the knowledge of the radiated power. Equation (2) refers to the specific problem approached in this paper, but the formulation is quite general because the field radiated by any antenna can be considered as incident field. It is worth noting that the analytical formulation of the phantom surfaces in Eq. (1) allows us to express all the geometrical parameters involved in the EM formulation in closed analytical form, which makes the algorithm very efficient from a computational point of view.

The calculation of the electric field reflected by the human body requires a preliminary analysis of the near and far field regions around the target. The field regions have been calculated for a human subject of 1.76 m at 23 GHz and 28 GHz, respectively. The results are listed in Table 2. The human target reflects the EM fields in far field starting from around 486 m and 591 m, at 23 GHz and 28 GHz,

**Table 2.** Near field and far field regions around a human target of size 1.76 m, analyzed at 23 GHz and at 28 GHz.

| Frequency $f$ (GHz) | Wavelength $\lambda$ (m) | Near field region $0.62\sqrt{D^3/\lambda}$ (m) | Far field region $2D^2/\lambda$ (m) |
|---|---|---|---|
| 23 | 0.013 | 12.68 | 474.96 |
| 28 | 0.011 | 13.98 | 578.21 |

respectively. The proposed EM tool has the aim to reproduce real scenes for detecting pedestrians, where the distances involved are less than 20 m [20]. Therefore, triangular patch surface meshes have been used to discretize the human body elements, representing each of them the equivalent sources for the scattered fields. Their sizes ($\Delta x, \Delta z \leq \lambda/10$) are chosen so that the scattering surface element $S$ is small enough to consider the currents uniform throughout, and the reflected field $E_n^s$ radiates in far field towards the antennas. $E_n^s$ is defined as

$$\vec{E}_n^s = \frac{\nabla\nabla \cdot \vec{A}}{j2\pi f \varepsilon \mu} - j2\pi f \vec{A} - \frac{1}{\varepsilon} \nabla \wedge \vec{F} \tag{3}$$

with $\vec{A}$ and $\vec{F}$ denoting the electric and magnetic potential vectors [40], and $\mu$ and $\varepsilon$ the permeability and permittivity of the analyzed body at the surface $S$. The total electric field scattered by the whole body is evaluated as superimposition of the radiation of each triangular patch [41].

$$\vec{E}^s = \sum_{n=1}^{N} \vec{E}_n^s \tag{4}$$

The computational details pertaining the approached problem based on the theory of the physical optics are reported in Appendix A.

## 3. RCS OF METAL AND LOSSY SPHERES AND OF A PEDESTRIAN IN THE K-BAND

The RCS of metal and lossy spheres and of a human target have been calculated in the frequency range 23–28 GHz. The objective is twofold: to determine the accuracy of the proposed simulation tool; to validate the our analytical approach for the RCS evaluation in the near field region. The simulated data have been compared with the experimental tests presented and discussed in [15] and with the theoretical results based on the Mie theory [12–14].

### 3.1. Simulation Setup

The RCS measurements have been performed in an anechoic chamber of the European Microwave Signature Laboratory (EMSL) by the European Commission Joint Research Centre [15]. The characteristics of the measurement setup and measurement site have been replicated in the simulation tool. The setup used in the RCS simulations is shown in Fig. 3.

The horn antennas (gain $G = 20$ dB at the center frequency) have been simulated by means of two rectangular apertures with dimensions $A_W$ and $A_H$ of 3.5 cm and 2.5 cm, respectively. The Tx and Rx antennas have been placed in quasi-monostatic configuration, with horizontal separation of about 15 cm between them. The polarization is vertical both for Tx and Rx antennas. The range distance between the antenna apertures to the rotation axis of the turntable is 3.4 m. The antennas have been placed at 1.1 m above the ground, as shown in Fig. 3.

### 3.2. RCS of Metal and Lossy Spheres

The first test focuses on the evaluation of the RCS of a perfectly conducting sphere. The result, provided by the proposed simulation tool, has been compared with the measured result presented in the report [15].

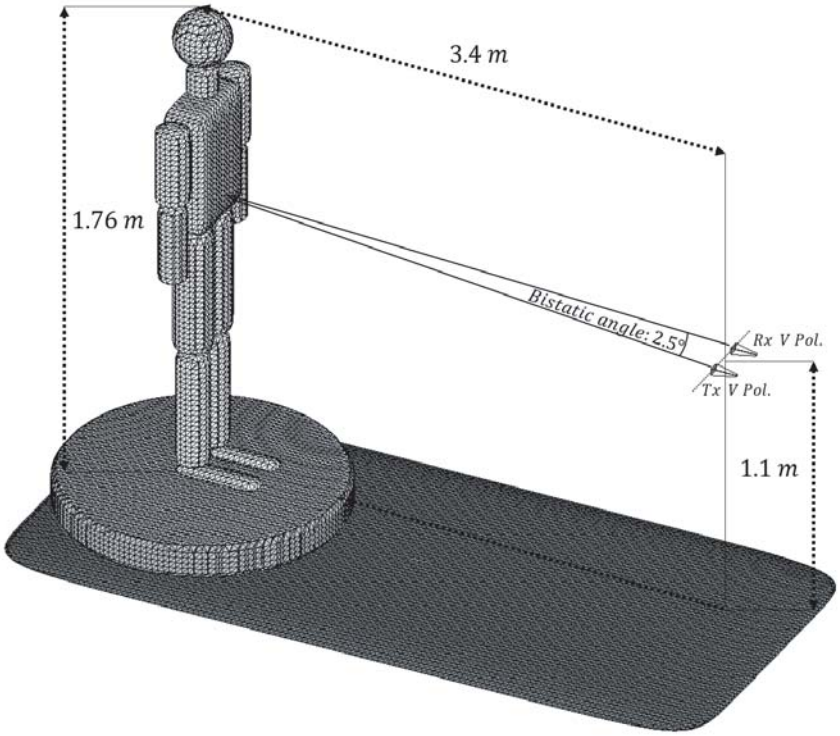

**Figure 3.** Setup for the evaluation of the RCS of a human target, reproduced in MATLAB® software.

A metal sphere with a radius 3.81 cm has been used for the test and placed at 3.4 m away the antennas. The sphere has been generated in the analytical model according to Equation (1), whereas the relative permittivity $\varepsilon_r = 1$ and conductivity $\sigma = 10^7$ S/m have been chosen for the metallic surface. The RCS of the sphere has been defined as follows

$$RCS_{sphere} = 4\pi R^2 \frac{|\vec{E}^s|}{|\vec{E}^i|} \tag{5}$$

$\vec{E}^i$ and $\vec{E}^s$ in Eq. (4) denote, respectively, the incident and reflected electric fields, and $R$ is the distance between the antennas and analyzed sphere. The results are shown in Fig. 4. The simulated RCS,

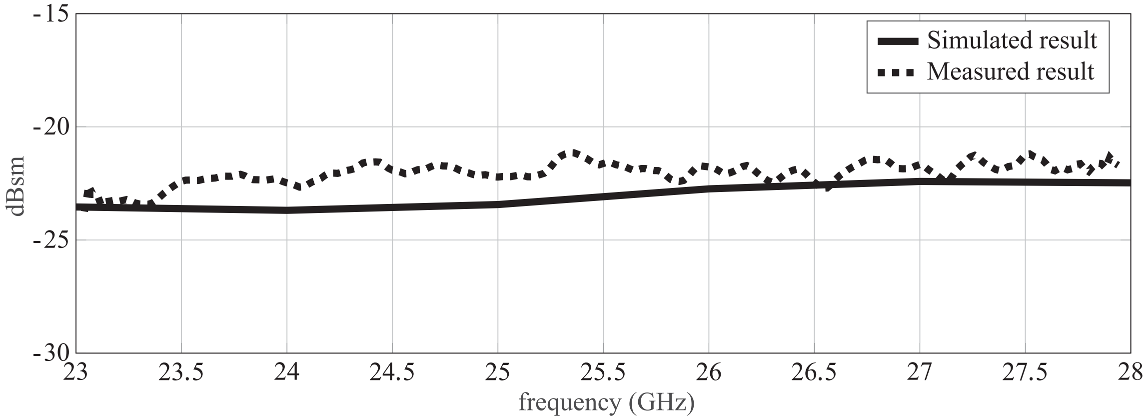

**Figure 4.** Comparison between the simulated (continuous line) and measured (dashed line) results relative to the RCS of a metal sphere in the frequency range 23–28 GHz.

continuous line, exhibits a monotonic increasing behavior from −23.5 dBsm to −22.5 dBsm, compared to a slightly oscillatory profile of the measured RCS, represented by the dashed line. Nevertheless, the response predicted by the proposed model can be considered in good agreement with the measurement, despite that a difference of approximately 2 dBsm is observed in the sub-band 24–26 GHz. In order to verify whether the discrepancy is due to the uncertainty of the measurement or an error in the proposed model, further tests have been performed to assess its accuracy.

In detail, the RCS of a metal and lossy sphere of radius 3.81 cm have been calculated and compared with the theoretical ones obtained by using the Mie series [12–14]. The dielectric properties of the lossy sphere correspond to those of the dry skin in the frequency band 23–28 GHz [37], whose values are listed in Table 3. The results are shown in Fig. 5. The simulated (continuous line) and theoretical (dotted line) radar cross sections of the PEC sphere vary approximately between −23.75 dBsm and −23 dBsm, and between −26.75 dBsm and −26.5 dBsm for the lossy sphere, as shown in Fig. 5(a) and Fig. 5(b), respectively. The results provided by our EM tool and those calculated by using the Mie series are in total agreement, observing at most a difference less than 0.3 dBsm for the PEC sphere and less than 0.25 dBsm for the lossy one. In the end, the accuracy of our simulation model has been tested analyzing the RCS of a PEC and lossy sphere of radius 10 cm. The spheres have been placed at 3.4 m and 25 m from the antennas. The two distances denote a near field and far field regions considering the diameter of the sphere the largest dimension of the chosen system. The simulated and theoretical results are depicted in Fig. 6. They exhibit a sinusoidal oscillation, ranging between −15.25 dBsm and −14.75 dBsm for the PEC sphere (Fig. 6(a)) and between −18.5 dBsm and 18 dBsm for the lossy sphere (Fig. 6(b)). The simulated RCS is in accordance with the RCS calculated by the Mie series,

**Table 3.** Dielectric properties of the dry skin in the frequency band 23–28 GHz.

| Frequency (GHz) | $\varepsilon_r$ | $\sigma$ (S/m) |
|---|---|---|
| 23 | 19.7 | 22 |
| 24 | 19 | 22.8 |
| 25 | 18.3 | 23.6 |
| 26 | 17.7 | 24.4 |
| 27 | 17.1 | 25.1 |
| 28 | 16.6 | 25.8 |

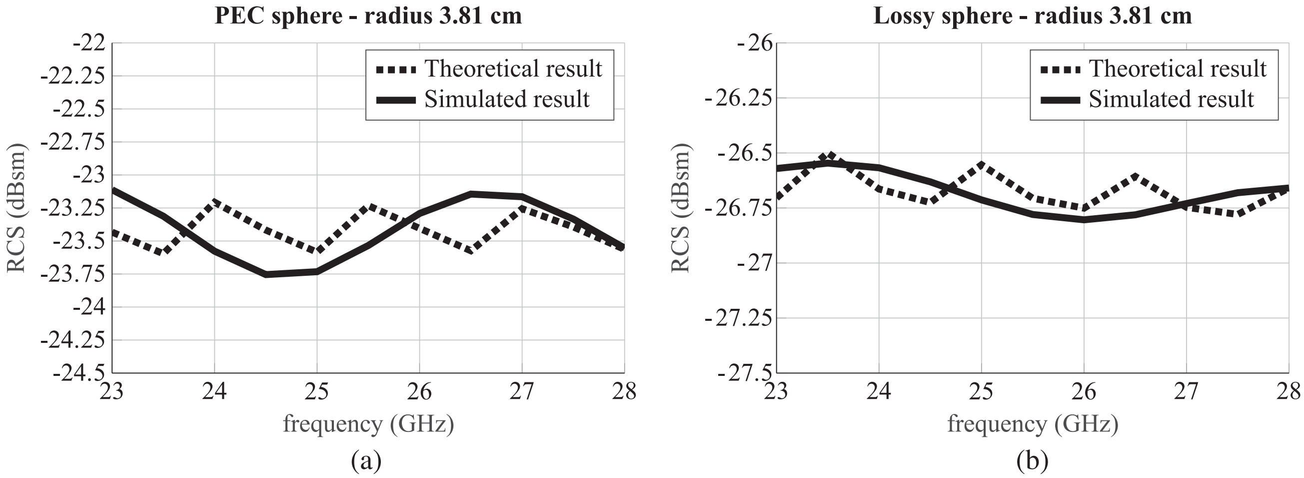

**Figure 5.** Comparison between the simulated (continuous line) and the theoretical (dotted line) results relative to the RCS of a sphere of radius 3.81 cm, analyzed in the frequency band 23–28 GHz: (a) PEC sphere, (b) lossy sphere.

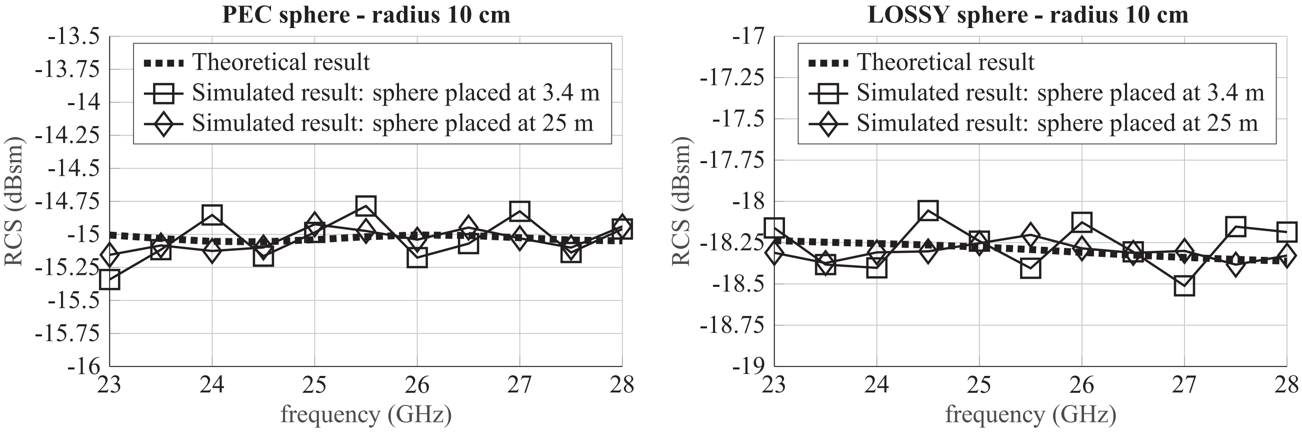

(a) (b)

**Figure 6.** Comparison between the simulated (continuous line) and the theoretical (dotted line) results relative to the RCS of a sphere of radius 10 cm, analyzed in the frequency band 23–28 GHz: (a) PEC sphere, (b) lossy sphere.

whatever chosen material and distance, observing a negligible error less than 0.25 dBsm. Thus, the tests highlight that the proposed model proves to be adequate for an accurate RCS evaluation of PEC and lossy homogeneous objects.

### 3.3. RCS of a Human Standing

The calculation of the RCS of a human subject has been carried out as a further test to assess the accuracy of the EM tool. The simulated results have been compared with the measured results presented in [15]. The sizes of the volunteer have not been provided in [15]. Therefore, a 3D human body with a total height of 1.76 m has been implemented. The human body parts have been modelled as described in Section 2 and their sizes, listed in Table 1, have been chosen to be equivalent to the average human body sizes [21–24]. The distance between the human 3D model and the antennas is 3.4 m, which identifies a near field region considering the chosen dimensions of the body and the frequency range. The measurements [15] have highlighted a negligible impact of the clothing on the RCS signature of the observed pedestrian. Consequently, they have not been taken into account in the simulations. The relative permittivity $\varepsilon_r$ and conductivity $\sigma$ listed in Table 3 have been assumed to simulate the dielectric properties of the dry skin in the frequency band 23–28 GHz [37].

The simulation tool collects the RCS pattern of 360 azimuth positions by rotating the human standing at step size of 1 degree. The comparison between the simulated and measured results has been carried out, evaluating within five sub-bands the global frequency azimuth average of the RCS, expressed as follows

$$R^{avg}_{i\text{-}band} = \frac{1}{M}\sum_{k=1}^{M} R^{\phi\text{-}avg}_{i\text{-}band}\left(\phi_k\right) \tag{6}$$

$M$ is the number of observed azimuth positions and $R^{\phi\text{-}avg}_{i\text{-}band}(\phi_k)$ the frequency average of the back scattered RCS. $R^{\phi\text{-}avg}_{i\text{-}band}(\phi_k)$ is defined as follows

$$R^{\phi\text{-}avg}_{i\text{-}band}\left[\phi\right] = \frac{1}{N}\sum_{j=1}^{N} \mid RCS\left(f_j\right) \mid \tag{7}$$

where $N$ denotes the total number of frequency points in the $i$-th sub-band spanning 1 GHz. $RCS(f_j)$ is given by

$$RCS\left(f\right) = \frac{S_{21}^2\left(f\right)\left(4\pi\right)^3 R^4}{G^2\left(f\right)\lambda^2\left(f\right)} \tag{8}$$

$G$ is the gain of the Tx and Rx antennas, $\lambda$ the wavelength relative to each frequency sample, and $R$ the distance between the antennas and the target. $S_{21}$ is the $S$-parameter of the system defined as

$$S_{21} = \frac{\vec{E}^s}{\sqrt{\frac{2\eta_0 P_t}{A_W A_H}}} \tag{9}$$

where $\eta_0$ represents the characteristic impedance of free space and $P_t$ the transmitting power corresponding to 0 dBm. $\vec{E}^s$ in Eq. (4) is the total electric field reflected by the human body, calculated as the sum of the electric fields scattered by each triangular patch $\vec{E}^s_n$ in Eq. (3). $\vec{E}^s_n$ is radiated toward the antennas in far field region considering the size of the mesh the largest dimension of the chosen sub-system. In addition, the real distance between the center of the triangular patch and the center of the antenna aperture is considered for the evaluation of each field contribution $\vec{E}^s_n$. This allows to take into account the correct phase and amplitude of the field.

Table 4 shows the results provided by the EM tool and by the experimental tests presented in [15]. The results computed by the simulation tool and experimental data are in a quite good agreement, observing at most a difference of 1.5 dB in the analyzed sub-bands.

**Table 4.** Global frequency azimuth average of the simulated and measured RCS of a human standing.

| Sub-band | Start Freq. (GHz) | Stop Freq. (GHz) | Measured [15] (dBsm) | Simulated (dBsm) |
|---|---|---|---|---|
| 1st | 23.0 | 24.0 | −4.37 | −5.67 |
| 2nd | 24.0 | 25.0 | −3.89 | −5.52 |
| 3rd | 25.0 | 26.0 | −4.15 | −5.32 |
| 4th | 26.0 | 27.0 | −3.75 | −5.27 |
| 5th | 27.0 | 28.0 | −3.78 | −5.49 |

The longitudinal and lateral positions of a pedestrian relative to an approaching vehicle influence the detection performed by the short-range radar systems [20]. Therefore, the RCS pattern has been further analyzed considering the main look angles of the potential pedestrian relative to the radars, in the band 23–28 GHz. The regions of the observation angles are labelled in Fig. 7. The simulated and measured results are shown in Fig. 8. The average values corresponding to the front, rear, and side viewing angles are listed in Table 5.

**Table 5.** Simulated and measured average values of the the pedestrian look angles.

| Look angles | Measured [15] (dBsm) | Simulated (dBsm) |
|---|---|---|
| Front | −5.47 | −5.26 |
| Rear | −2.19 | −5.49 |
| Right side | −3.90 | −5.53 |
| Left side | −4.97 | −5.36 |

The simulated data prove to be in good agreement with those measured concerning the front and left view angles of the target, observing at most a difference of 0.38 dBsm. The differences occur instead analyzing the rear and right look angles as highlighted in Table 5. In detail, a difference in average of 1.6 dBsm with a maximum value of 3.2 dBsm is observed between the measured and simulated results in the interval 115°–260°, as shown in Fig. 8. However, in the authors' opinion, a comparison between simulated and measured RCS values for each angular sample is not particularly significant, as the

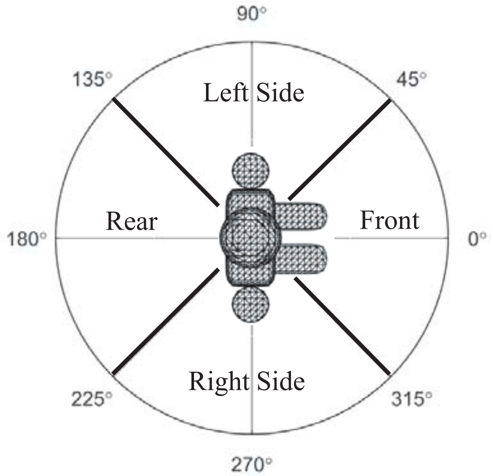

**Figure 7.** Reference of the standing pedestrian look angles.

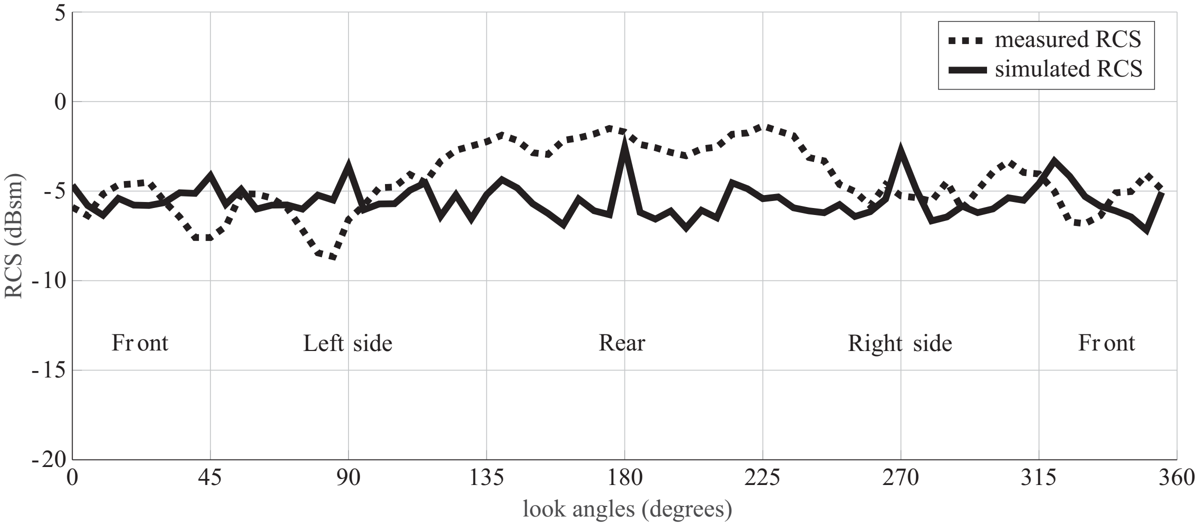

**Figure 8.** Simulated (continuous line) and measured [15] (dashed line) RCS pattern of a human standing in the frequency band 23–28 GHz.

measurements are affected by many random errors. This can be easily verified observing, for example, that no symmetry can be found in the experimental data, even if a human body shows a left side/right side symmetry. The differences may be associated with the involuntary movements of the human subject during the rotation of the turntable, which affect the experimental evaluation and cannot be predicted in the simulation. The position changes of the subject have also been observed by Lemmen et al. in [43].

To highlight this aspect, further simulations have been carried out to evaluate the influence of involuntary displacements of the human target on the RCS signature. In detail, in the range 115°–260°, the 3D human model has been placed at different distances respect to the antennas in order to simulate involuntary movements. Then, a full 360 degree RCS pattern has been calculated by the EM tool. The results from varying the standing position of a human are depicted by markers in Fig. 9 and superimposed to the measured and simulated results already observed in Fig. 8. The agreement between the experimental data and those provided by the proposed EM tool is improved. Nevertheless, a difference between the measured result and simulated data is still detected in the azimuth positions 120°–170° and 200°–240°. It is worth noting that involuntary oscillations of the target determine large fluctuations in the received power due to the use of millimeter waves. Small changes of the position of the body with respect to the incident wave cause an uncertainty on the retrieved RCS of several dB. These displacements are unpredictable at the numerical modeling stage, and consequently a punctual comparison between the simulated and measured RCS patterns becomes a difficult task. Proper knowledge of the sizes of the target and of its placement in the observed scenario could improve the accuracy of the data provided by the simulation tool.

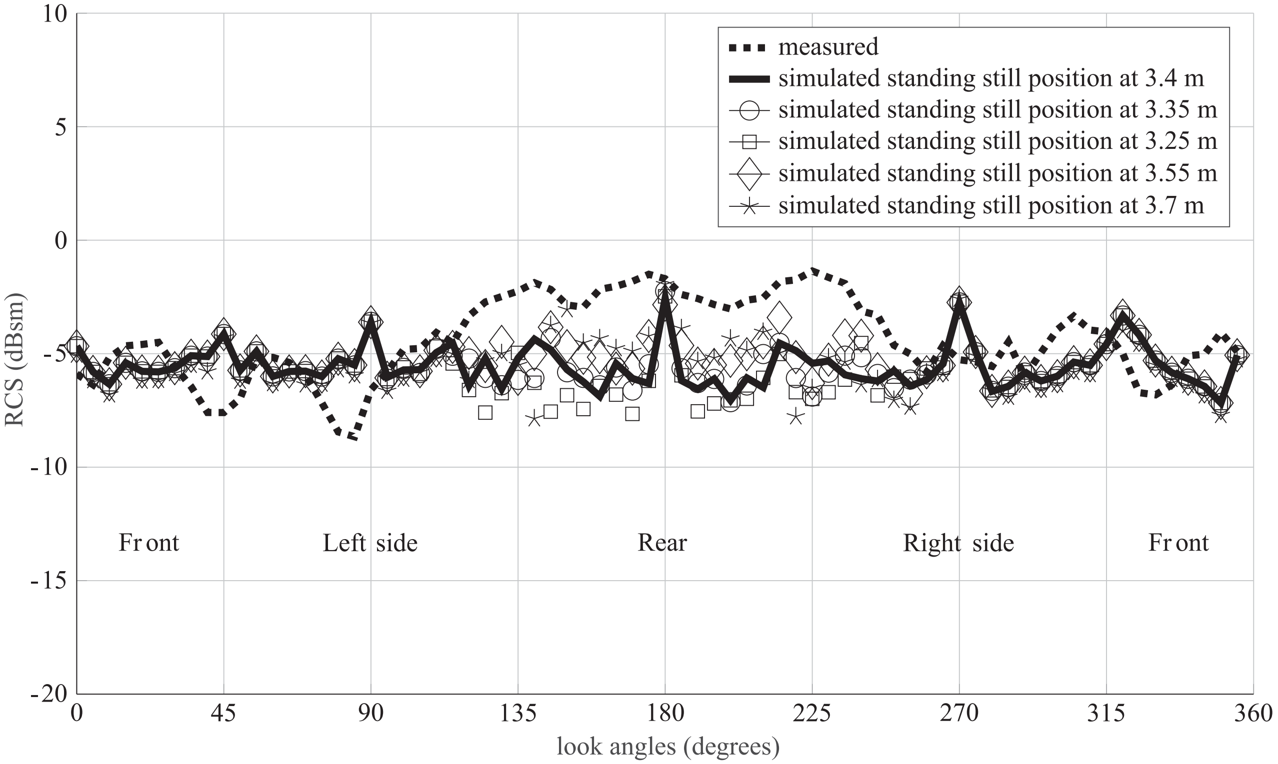

**Figure 9.** Comparison between measured and simulated RCS of a human target, in the frequency band 23–28 GHz. Measured result [15] (dashed line), simulated results of a human placed at 3.4 m away the antennas (continuous line), and at different positions (markers).

## 4. PERFORMANCE ASSESSMENT

The performance of the proposed EM tool has been assessed and compared with those of two numerical solutions, FDTD and MLFMM, available in the commercial simulation tool FEKO$^{\text{TM}}$. To this purpose, the RCS of a perfectly conductive sphere has been analyzed at 24 GHz. A diameter of 20 cm has been chosen close to the average size of a human head [21–24]. A coarse meshing ($\lambda/8$) has been used to model the sphere in FEKO$^{\text{TM}}$, representing a good tradeoff between the simulation accuracy and simulation speed. The meshing type has also been adopted on the proposed model. The simulations have been carried out by using a computer whose feature are: processor Intel Xeon CPU E3-1270 v6 (clock rate 3.8 GHz), 64 GByte RAM DDR4, graphics card INVIDIA QUADRO M2000 4 GByte GDDR5.

The number of meshes, the CPU time, the memory usage demanded by the used numerical solutions, and the RCS values of the metal sphere at 24 GHz are shown in Table 6. The result provided by the our model agrees with those calculated by using the MLFMM and FDTD methods with a negligible error of 0.33 dBsm. The calculation of the RCS of the sphere has required 30 s and 1.55 GByte of memory. Therefore, the EM tool proves to be both sufficiently accurate and efficient from the point of view of the computational burden compared with the numerical solutions available in FEKO$^{\text{TM}}$.

**Table 6.** Computational demands on analyzing the RCS of a metal sphere at 24 GHz, by using FDTD method, MLFMM and a PO-based EM tool.

| EM solvers | Meshes | CPU time (HH:MM:SS) | Used RAM | RCS |
|---|---|---|---|---|
| FDTD (FEKO$^{\text{TM}}$) | 35611289 | 01:17.15 | 4.25 Gbyte | −15.36 dBsm |
| MLFMM (FEKO$^{\text{TM}}$) | 313860 | 13:22:43 | 2.73 GByte | −15.13 dBsm |
| Proposed EM tool | 154256 | 00:00:30 | 1.55 Gbyte | −15.03 dBsm |

vskip0.05in

## 5. CONCLUSION

The paper presents the development of a simulation tool based on a human body model analytically described and the technique of PO theory, to characterize the scattered field in K-band. The algorithm has been implemented in MATLAB® software, generating a simulation tool, which presents three main strengths. The EM tool includes the modeling of the human body, analytically expressed, avoiding the use of external software packages. The use of elementary shapes allows one to develop a 3D human model with a good resolution and without any significant distortion of the back-scattered waveform. The field radiated by any antenna can be considered as incident field, allowing a more faithful modelling of the observed scene, compared to the use of a plane wave source. The tool allows one to analyze scenarios involving a large problem space, without the need of HPC systems.

The comparison between the experimental and numerical data verifies the validity of the proposed EM tool, for both the evaluation of the RCS of PEC and lossy homogeneous dielectric shapes. The simulation tool proves to be light from the point of view of computational burden, and more efficient than widely used numerical tools, which usually face the huge computation time involved in detailed modeling of the human body.

In the end, the EM model proves to be suitable for the analysis of different pedestrian scenarios. For instance, the analysis of the RCS of a pedestrian performing a physical activity such as running or walking can be carried out. Moreover, the influence of metal accessories, such as a watch or a bracelet worn by the pedestrian, on the RCS signature can also be assessed.

## ACKNOWLEDGMENT

The authors wish to thank Eng. Joaquim Fortuny-Guasch of the Joint Research Centre (JRC) of Ispra, for his valuable availability and concession of the measured data files performed in the JRC.

## APPENDIX A.

The detailed procedures to calculate $TE$ and $TM$ components of the electric and magnetic fields tangential to the surface $S$ are provided in the following section.

### A.1. TE and TM Components

The evaluation of the field scattered by the equivalent source requires the knowledge of the incident electric $\vec{E}^i$ and magnetic $\vec{H}^i$ fields, radiated by the antenna in far field conditions. $\vec{E}^i$ and $\vec{H}^i$ are orthogonal to $\hat{r}$ and represented in $TE$ and $TM$ components to evaluate their interaction with the body. The reflected fields are calculated on each mesh [42], considering the oblique incidence of a plane-wave on the interface air/skin, as depicted in Fig. A1.

The total electric field, tangential to the surface $S$ and due to the $TE$ components, is given by

$$\vec{E}_{\tan}^{TE} = \left(1 + \rho^{TE}\right) \left(\vec{E}^i \cdot \hat{v}\right) \hat{v} \tag{A1}$$

And the $TM$ component is

$$\vec{E}_{\tan}^{TM} = \left(1 - \rho^{TM}\right) \left[\left(\vec{E}^i - \vec{E}^{TE}\right) \cdot \hat{\tau}\right] \hat{\tau} \tag{A2}$$

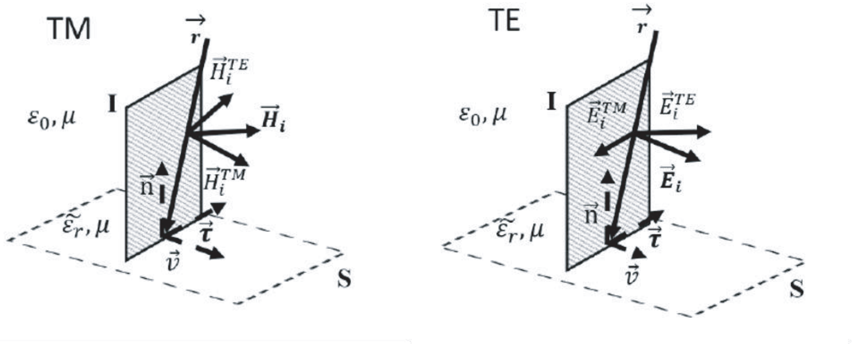

**Figure A1.** Oblique incidence of electric and magnetic fields.

Similarly, the $TM$ magnetic field component is

$$\vec{H}^{TM}_{\tan} = \left(1 + \rho^{TM}\right)\left(\vec{H}^i \cdot \hat{v}\right)\hat{v} \tag{A3}$$

and the $\vec{H}^{TE}$ component is

$$\vec{H}^{TE}_{\tan} = \left(1 - \rho^{TE}\right)\left[\left(\vec{H}^i - \vec{H}^{TM}\right)\cdot\hat{\tau}\right]\hat{\tau} \tag{A4}$$

where

$$\rho^{TE} = \frac{\cos\theta_i - \sqrt{\left(\varepsilon_r - \dfrac{j\sigma}{\omega\varepsilon_0}\right) - 1 + \cos\theta_i{}^2}}{\cos\theta_i + \sqrt{\left(\varepsilon_r - \dfrac{j\sigma}{\omega\epsilon_0}\right) - 1 + \cos\theta_i{}^2}} \tag{A5}$$

$$\rho^{TM} = \frac{\sqrt{\left(\varepsilon_r - \dfrac{j\sigma}{\omega\varepsilon_0}\right) - 1 + \cos\theta_i{}^2} - \left(\varepsilon_r - \dfrac{j\sigma}{\omega\varepsilon_0}\right)\cos\theta_i}{\sqrt{\left(\varepsilon_r - \dfrac{j\sigma}{\omega\varepsilon_0}\right) - 1 + \cos\theta_i{}^2} + \left(\varepsilon_r - \dfrac{j\sigma}{\omega\varepsilon_0}\right)\cos\theta_i} \tag{A6}$$

$$\cos\theta_i = -\hat{n}_i \cdot \hat{r}_i \tag{A7}$$

$\rho^{TE}$ and $\rho^{TM}$ are the reflection coefficients, and $\theta_i$ is the incidence angle. $\varepsilon_r$ and $\sigma$ represent the relative permittivity and conductivity of the analyzed body at the surface $S$. The knowledge of the electric and magnetic fields on $S$ allows one to determine the equivalent electric $\vec{J}$ and magnetic $\vec{M}$ surface current densities for the evaluation of the scattered field.

$$\vec{J} = \hat{n} \wedge \left(\vec{H}^{TE}_{\tan} + \vec{H}^{TM}_{\tan}\right) \tag{A8}$$

$$\vec{M} = \left(\vec{E}^{TE}_{\tan} + \vec{E}^{TM}_{\tan}\right) \wedge \hat{n} \tag{A9}$$

## REFERENCES

1. Fleming, B., "New automotive electronics technologies [automotive electronics]," *IEEE Vehicular Technology Magazine*, Vol. 7, No. 4, 4–12, 2012.
2. Euro NCAP — Autonomous Emergency Breaking, `https://tinyurl.com/yy2ec6ew`, date last accessed 20-Jan.-2020.
3. Langer, D. and T. Jochem, "Fusing radar and vision for detecting, classifying and avoiding roadway obstacles," *Proceedings of the 1996 IEEE Intelligent Vehicles Symposium, 1996*, 333–338, 1996.

4. Kato, T., Y. Ninomiya, and I. Masaki, "An obstacle detection method by fusion of radar and motion stereo," *IEEE Transactions on Intelligent Transportation Systems*, Vol. 3, No. 3, 182–188, 2002.
5. Park, M. K., S. Y. Lee, C. K. Kwon, and S. W. Kim, "Design of pedestrian target selection with funnel map for pedestrian AEB system," *IEEE Transactions on Vehicular Technology*, Vol. 66, No. 5, 3597–3609, 2017.
6. Sakamoto, T., T. Sato, P. J. Aubry, and A. G. Yarovoy, "Texture-based automatic separation of echoes from distributed moving targets in UWB radar signals," *IEEE Transactions on Geoscience and Remote Sensing*, Vol. 53, No. 1, 352–361, 2015.
7. Chang, S., R. Sharan, M. Wolf, N. Mitsumoto, and J. W. Burdick, "UWB radar-based human target tracking," *2009 IEEE Radar Conference*, 1–6, 2009.
8. Okumura, S., T. Sato, T. Sakamoto, and T. Sato, "Technique of tracking multiple pedestrians using monostatic ultra-wideband Doppler radar with adaptive Doppler spectrum estimation," *2016 International Symposium on Antennas and Propagation (ISAP)*, 320–321, 2016.
9. Yamada, N., Y. Tanaka, and K. Nishikawa, "Radar cross section for pedestrian in 76 GHz band," *2005 European Microwave Conference*, 4–1018, 2005.
10. Marchetti, E., R. Du, F. Norouzian, E. G. Hoare, T. Y. Tran, M. Cherniakov, and M. Gashinova, "Comparison of pedestrian reflectivities at 24 and 300 GHz," *2017 18th International Radar Symposium (IRS)*, 1–7, 2017.
11. Chen, M. and C. Chen, "RCS Patterns of Pedestrians at 76–77 GHz," *IEEE Antennas and Propagation Magazine*, Vol. 56, No. 4, 252–263, 2014.
12. Ruck, G. T., D. E. Barrick, W. D. Stuart, and C. K. Krichbaum, *Radar Cross Section Handbook*, Plenum Press, New York, 1970.
13. Knott, E. F., *Radar Cross Section Measurements*, Springer Science & Business Media, 2012.
14. "Scattered field of a conducting and stratified sphere," https://it.mathworks.com/matlabcentral/fileexchange/20430-scattered-field-of-a-conducting-and-stratified-spheres, date last accessed 20-Jan.-2020.
15. Fortuny-Guasch, J. and J. M. Chareau, "Radar cross section measurements of pedestrian dummies and humans in the 24/77 GHz frequency bands: Establishment of a reference library of RCS signatures of pedestrian dummies in the automotive radar bands," 2013.
16. Le, C. and T. Dogaru, "Numerical modeling of the airborne radar signature of dismount personnel in the UHF-, L-, Ku-, and Ka-bands," *Army Research Lab Adelphi MD and Electron Devices Directorate*, 2007.
17. Ur-Rehman, M., Q. H. Abbasi, X. Chen, and Z. Ying, "Numerical modelling of human body for Bluetooth body-worn applications," *Progress In Electromagnetics Research*, Vol. 143, 623–639, 2013.
18. Dogaru, T. and C. Le, "Validation of Xpatch computer models for human body radar signature," *Army Research Lab Adelphi MD and Electron Devices Directorate*, 2008.
19. Yi, X., G. Feng, Z. Liang, C. Wang, B. Liu, C. Li, K. Yang, C. C. Boon, and Q. Xue, "A 24/77 GHz dual-band receiver for automotive radar applications," *IEEE Access*, Vol. 7, 48053–48059, 2019.
20. Hamdane, H., T. Serre, C. Masson, and R. Anderson, "Issues and challenges for pedestrian active safety systems based on real world accidents," *Accident Analysis & Prevention*, Vol. 82, 53–60, 2015.
21. Chen, M., C. C. Chen, S. Y.-P. Chien, and R. Sherony, "Artificial skin for 76–77 GHz radar mannequins," *IEEE Transactions on Antennas and Propagation*, Vol. 62, No. 11, 5671–5679, 2014.
22. Schwind, A., R. Stephan, and M. A. H. Thuringian, "Simulations and measurements of the bistatic radar cross section of vulnerable road users between 2 GHz and 6 GHz," *2018 IEEE MTT-S International Conference on Microwaves for Intelligent Mobility (ICMIM)*, 1–4, 2018.
23. Lee, S., Y. Yoon, J. Lee, and S. Kim, "Human-vehicle classification using feature-based SVM in 77-GHz automotive FMCW radar," *IET Radar, Sonar Navigation*, Vol. 11, No. 10, 1589–1596, 2017.

24. Poston, A., *Human Engineering Design Data Digest: Human Factors Standardization Systems*, Human Factors Standardization SubTAG, 2000.
25. 3D CAD Browser, https://www.3dcadbrowser.com, date last accessed 20-Jan.-2020.
26. REMCOM — VariPose, https://www.remcom.com/xf-varipose-biological-mesh-repositioning, date last accessed 20-Jan.-2020.
27. MakeHuman — Open Source tool for making 3-D characters, http://www.makehumancommunity.org, date last accessed 20-Jan.-2020.
28. Basar, M. R., F. Malek, K. M. Juni, M. I. M. Saleh, M. S. Idris, L. Mohamed, N. Saudin, N. A Mohd Affendi, and A. Ali, "The use of a human body model to determine the variation of path losses in the human body channel in wireless capsule endoscopy," *Progress In Electromagnetics Research*, Vol. 133, 495–513, 2013.
29. Van Dorp, P. and F. C. A. Groen, "Human walking estimation with radar," *IEE Proceedings — Radar, Sonar and Navigation*, Vol. 150, No. 5, 356–365, 2003.
30. Mohamed, M., M. Cheffena, F. P. Fontan, and A. Moldsvor, "A dynamic channel model for indoor wireless signals: Working around interference caused by moving human bodies," *IEEE Antennas and Propagation Magazine*, Vol. 60, No. 2, 82–91, 2018.
31. Autodesk — M Maya, https://www.autodesk.com/products/maya/overview, date last accessed 20-Jan.-2020.
32. Chen, M., M. Kuloglu, and C. Chen, "Numerical study of pedestrian RCS at 76–77 GHz," *2013 IEEE Antennas and Propagation Society International Symposium (APSURSI)*, 1982–1983, 2013.
33. Belgiovane, D., C. Chen, M. Chen, S. Y. Chien, and R. Sherony, "77 GHz radar scattering properties of pedestrians," *2014 IEEE Radar Conference*, 0735–0738, 2014.
34. De Leo, A., V. M. Primiani, P. Russo, D. Shahu, V. Di Mattia, and G. Cerri, "Breath detection of humans buried in a homogeneous lossy medium: A simplified analytical model," *2012 International Symposium on Electromagnetic Compatibility (EMC EUROPE)*, 1–6, 2012.
35. Manfredi, G., V. Di Mattia, P. Russo, A. De Leo, and G. Cerri, "The human body modelled by canonical geometric shapes for the analysis of scattered E-fields," *Applied Computational Electromagnetics Society Journal*, Vol. 33, No. 7, 741–745, 2018.
36. Tamyis, N. M., D. K. Ghodgaonkar, M. N. Taib, and W. T. Wui, "Dielectric properties of human skin in vivo in the frequency range 20–38 GHz for 42 healthy volunteers," *Proceedings of the 28th URSI General Assembly*, 23–29, 2005.
37. Istituto di Fisica Appliccata "Nello Carrara" — Dielectric properties of body tissues, http://niremf.ifac.cnr.it/tissprop/htmlclie/htmlclie.php, date last accessed 20-Jan.-2020.
38. Asvestas, J. S., "The physical optics method in electromagnetic scattering," *Journal of Mathematical Physics*, Vol. 21, No. 2, 290–299, 1980.
39. Akhmanov, S. A. and S. Y. Nikitin, *Physical Optics*, Clarendon Press, 1997.
40. Balanis, C. A., *Antenna Theory: Antenna and Design*, John Wiley & Sons, 2005.
41. Barber, P. W. and C. Yeh, "Scattering of electromagnetic waves by arbitrarily shaped dielectric bodies," *Applied Optics*, Vol. 14, No. 12, 2864–2872, 1975.
42. Ramo, S., J. R. Whinnery, and T. Van Duzer, *Fields and Waves in Communication Electronics*, John Wiley & Sons, 2008.
43. Lemmen, P., J. Stoll, U. Bergelt, P. Seiniger, M. Wisch, O. Bartels, E. Schubert, M. Kunert, I. Knight, D. Brookes, et al., "Evaluation of pedestrian targets for use in automomous emergengy brake system testing-a report from the harmonistion platform 2 dealing with test equipment," *23rd Conference on the Enhancement of the Safety of Vehicles (ESV)*, 2013.